Ann. Geophys., 31, 463–471, 2013
www.ann-geophys.net/31/463/2013/
doi:10.5194/angeo-31-463-2013

Annales Geophysicae
Open Access

Thermospheric neutral temperatures derived from charge-exchange produced N_2^+ Meinel (1,0) rotational distributions

C. K. Mutiso, M. D. Zettergren, J. M. Hughes, and G. G. Sivjee

Space Physics Research Laboratory, Embry-Riddle Aeronautical University, Daytona Beach, FL, USA

Correspondence to: C. K. Mutiso (mutisoc@gmail.com)

Received: 12 November 2012 – Revised: 5 January 2013 – Accepted: 7 January 2013 – Published: 12 March 2013

Abstract. Thermalized rotational distributions of neutral and ionized N_2 and O_2 have long been used to determine neutral temperatures (T_n) during auroral conditions. In both bright E-region ($\lesssim$150 km) auroras, and in higher-altitude auroras, spectral distributions of molecular emissions employed to determine T_n in the E-region cannot likewise be used to obtain T_n in the F-region. Nevertheless, charge-exchange reactions between high-altitude ($\gtrsim$130 km) species provide an exception to this situation. In particular, the charge-exchange reaction $O^+(^2D) + N_2(X) \longrightarrow N_2^+(A^2\Pi_u,\ v' = 1) + O(^3P)$ yields thermalized N_2^+ Meinel (1,0) emissions, which, albeit weak, can be used to derive neutral temperatures at altitudes of ∼130 km and higher.

In this work, we present N_2^+ Meinel (1,0) rotational temperatures and brightnesses obtained at Svalbard, Norway, during various auroral conditions. We calculate T_n at thermospheric altitudes of 130–180 km from thermalized rotational populations of N_2^+ Meinel (1,0); these emissions are excited by soft electron ($\lesssim$1 keV) impact and charge-exchange reactions. We model the contributions of the respective excitation mechanisms, and compare derived brightnesses to observations. The agreement between the two is good. Emission heights obtained from optical data, modeling, and ISR data are consistent. Obtaining thermospheric T_n from charge-exchange excited N_2^+ Meinel (1,0) emissions provides an additional means of remotely sensing the neutral atmosphere, although certain limiting conditions are necessary. These include precipitation of low-energy electrons, and a non-sunlit emitting layer.

Keywords. Atmospheric composition and structure (Airglow and aurora) – Ionosphere (Auroral ionosphere; Instruments and techniques)

1 Introduction

Determining the temperature is one of the primary measurements undertaken in atmospheric remote sensing. Tropospheric and stratospheric temperatures are key reflectors of ozone and greenhouse gas levels, both of which directly influence global climate. Similarly, mesospheric temperatures play an important role in the study of gravity waves, which are fundamental in understanding global atmospheric dynamics.

In the troposphere, stratosphere, and mesosphere, radiosondes have been used extensively to directly measure temperatures. In a study spanning several decades, Angell and Korshover (1983) determined global temperature means at several altitudes in the range 1–20 km. Temperatures at similar altitudes have also been derived using mesosphere-stratosphere-troposphere (MST) radars (Matuura et al., 1986; Revathy et al., 1996) and atmospheric lidars (Chanin and Hauchecorne, 1981; Keckhut et al., 2001).

In the mesopause (∼87 km) and upper mesosphere, metallic ions and atoms deposited by meteors enable high-resolution neutral temperature calculations. Once again, lidars (e.g., She et al., 1993) and meteor radars (e.g., Hocking and Hocking, 2002) play a key role. Spectroscopy of the OH radical (Kvifte, 1961; Sivjee and Hamwey, 1987) is another longstanding method used to sense temperatures in the mesopause.

Above the mesopause, ionization by photons, electrons, and protons gives rise to the ionosphere, and no single temperature characterizes this region. Instead, the kinetic temperatures of ions and electrons (T_i and T_e, respectively), and the rotational temperature (T_{rot}) of the neutrals (T_n) must be obtained with multiple instruments (T_{rot} = T_n assuming local thermodynamic equilibrium). Incoherent scatter radars

routinely derive T_i and T_e profiles from 100 to 500 km (Kelly, 1983), and several methods are employed to determine T_n in the same altitude range.

At heights of ∼97 km, Fabry–Perot interferometers (Hernandez, 1976) infer T_n from the Doppler broadening of O(^{1}S) 557.7 nm. This same technique applied to O(^{1}D) 630.0 nm provides neutral temperatures at ∼240 km (Killeen et al., 1995). The most established remote-sensing technique, however, for obtaining T_n in the range 100–500 km, involves spectrometry. Since the early 1930s, T_n has been obtained from N_2 and N_2^+ rotational distributions, initially through spectrophotometry of N_2^+ 1st Negative bands (Vegard, 1932), and subsequently for F-region heights from the N_2 Vegard–Kaplan bands (Petrie, 1953). Neutral temperatures have also been derived from the following N_2^+ bands: N_2^+ 1st Negative (1N) (0,1): (e.g., Vegard, 1932; Romick et al., 1978; Koehler et al., 1981; Vallance Jones et al., 1987); 1N (0,2): (Jokiaho et al., 2008); 1N (1,2), (2,3) and Meinel (2,0): (Henriksen, 1984); 1N (0,3): (Henriksen et al., 1987); Meinel (0,0) and (1,0): (Espy et al., 1987; Sivjee et al., 1999).

This current work presents spectrometric N_2^+ Meinel (1,0) rotational temperatures and brightnesses obtained from a high-latitude station under various auroral conditions. We show how, in non-sunlit conditions, charge-exchange reactions (Espy et al., 1987; Sivjee et al., 1999), together with soft electron impact, both produce N_2^+ Meinel (1,0) emissions at altitudes $\gtrsim$130 km. We infer neutral temperatures (T_n) from the thermalized rotational spectra of these emissions, and identify challenges and limitations associated with interpreting the spectra. In order to elucidate the contribution of each excitation mechanism, we invert multi-wavelength optical measurements to retrieve the precipitating electron spectrum, which is then input into a forward model of the ionosphere, TRANSCAR (Lilensten and Blelly, 2002; Diloy et al., 1996; Blelly et al., 1996). We compare modeled emission brightnesses with observations, and estimate the N_2^+ Meinel (1,0) emission heights using several methods.

Contrasted with the nighttime results are time series of N_2^+ Meinel (1,0) rotational temperatures obtained under the cusp, when electron impact, charge exchange, and resonant scattering all excite the emission. We show that, in sunlit conditions, resonant scattering of the N_2^+ ion leads to marked differences between T_{rot} and T_n, precluding the calculation of neutral temperatures from N_2^+ rotational spectra. Time series of select O and O^+ emissions and geomagnetic indicators provide contextual background and aid in the comparison of the two sets of results.

This work is laid out as follows: Sect. 2 describes the instrumentation, consisting of an optical spectrometer, and provides experiment details. An overview of the TRANSCAR model is provided in Sect. 3. Next, Sect. 4 briefly introduces the N_2^+ Meinel emission, listing the various excitation processes pertinent to this work. Section 5 presents the main results, and a discussion and summary conclude the paper.

2 Instrumentation and experiment details

The Kjell Henriksen Observatory in Breinosa, Svalbard (78.15° N, 16.04° E, invariant latitude $\Lambda = 76°$ N) operates a suite of optical and radio instruments that monitor the polar cap mesosphere and thermosphere. This observatory is uniquely situated to study the dayside and cusp aurora.

Spectral signatures of auroral emissions above Svalbard were obtained using a 0.5-m focal length, $f/4.5$ modified Czerny-Turner grating spectrometer in the winter of 2007. The instrument is fitted with a charge coupled device (CCD) camera to detect optical spectra in the near infrared (700.0 to 950.0 nm), and is optimized for low-level light detection through the use of large, highly reflective optics. Light from a 12° circular field of view in the magnetic zenith enters the spectrometer via an order-sorting filter and a curved, 45-mm arc length Fastie slit. An adjustable slit width of 0.5 mm provides an acceptable compromise between throughput and spectral resolution. A 0.5-m focal length spherical mirror collimates and reflects the incoming rays onto a 110 mm × 110 mm, 1200 grooves mm^{-1} plane diffraction grating. An $f/1.4$, 85-mm focal length compound lens focuses the diffracted light onto the CCD detector. The detector is thermoelectrically cooled; this, in conjunction with a liquid cooling unit, allows for low dark current and high signal-to-noise (S/N) ratios, both of which facilitate the detection of weak emission features.

When observing in first order, the spectrometer covers a free spectral range of ∼240.0 nm, yielding imaged spectral lines with a nominal full width at half maximum (FWHM) of 0.8–1.1 nm. Typical integration times last 120 s. An absolute spectral sensitivity calibration of the instrument was performed according to Sigernes et al. (2007).

Observations presented here were timed to coincide with the midwinter new-moon period in December 2007. The solar depression angle was never less than 11 degrees, thus allowing for uninterrupted measurements, including around local noon.

3 The TRANSCAR model

In Sect. 5.3, TRANSCAR (Lilensten and Blelly, 2002) is used to compare modeled and observed emission brightnesses, and to estimate the contributions of competing excitation processes to the overall N_2^+ Meinel (1,0) intensity. TRANSCAR is a 1-dimensional, time-dependent forward model of the ionosphere, consisting of dynamically coupled fluid and kinetic modules that together solve for the spatiotemporal distributions of the density, drift velocity, temperature, and heat flux for e^-, O^+, N_2^+, H^+, N^+, NO^+, and O_2^+. As inputs, it accepts background ionospheric conditions (plasma density, convection electric field, topside electron heat flux, among others), neutral densities and temperatures from MSIS-90 (Hedin, 1991), and select geomagnetic

indices. For auroral modeling, it is possible to specify time-varying precipitating electron distributions. The kinetic module (Lummerzheim and Lilensten, 1994) solves the transport equations for suprathermal electrons. Rates for chemical reactions are compiled from published reports. A complete description of the model is available in, for example, Lilensten and Blelly (2002); Diloy et al. (1996); Blelly et al. (1996); Zettergren (2009).

4 Background on the N_2^+ M emission

Two emissions from the N_2^+ ion are significant in aurora. Transitions from the $N_2^+(B)$ state to the $N_2^+(X)$ ground state form the extensively-studied 1st Negative (1N) band system in the ultraviolet. Meinel (1950) first identified the emissions associated with the $N_2^+(A) \rightarrow N_2^+(X)$ transitions; these bands are prominent in the infrared, with the brightest being the (1,0), (0,0), and (2,0) bands at 918.2 nm, 1108.7 nm, and 785.3 nm, respectively (Vallance Jones, 1974).

Ionization of N_2 is accomplished by three primary means: electron impact, and by photoionization and resonant scattering under sunlit conditions. An additional means of selective ionization is provided through charge-exchange reactions between O^+ and N_2 (Broadfoot, 1967; Broadfoot and Stone, 1999). Espy et al. (1987), on the basis of excess populations of $N_2^+(A^2\Pi_u,\ \nu' = 1)$ ions in comparison with $\nu' = 0, 2$ ions, have provided strong support that in aurora, the resonant charge exchange shown in Reaction (R1) selectively populates the $\nu' = 1$ level. Originally proposed by Omholt (1957) as a source of $N_2^+(A^2\Pi_u)$, the mechanism has been questioned by several parties (e.g., Vallance Jones, 1974), but recent work has established its importance (Espy et al., 1987; Sivjee et al., 1999; Broadfoot and Stone, 1999, and included references).

$$O^+(^2D) + N_2(X) \longrightarrow N_2^+(A^2\Pi_u,\ \nu' = 1) + O(^3P) \qquad \text{(R1)}$$

Thus, on the nightside, the lower E-region N_2^+ M ($\nu' = 1$) level is populated by hard electrons, while the same vibrational level at higher altitudes is populated both by soft electrons ($\lesssim$1 keV), and the charge-exchange Reaction (R1) (Sivjee et al., 1999). On the dayside and in the cusp, resonance absorption of sunlight is another important source (Broadfoot, 1967). The following section presents observations of N_2^+ M(1,0) emissions obtained from the latter three sources. Determining rotational temperatures from charge-exchange excited emissions provides an additional means of remotely sensing the upper E-region and F-region, but requires a non-sunlit emitting layer and precipitation of low-energy electrons. Under such conditions, ionization of the thermalized N_2 molecule does not alter its rotational distribution (Chamberlain, 1961); therefore, rotational spectra yield the neutral temperature averaged over the altitude distribution of the emitting layer.

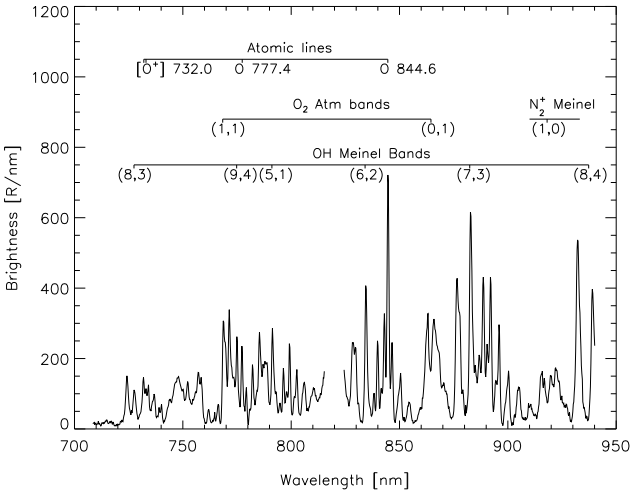

Fig. 1. A typical high-altitude auroral spectrum from Svalbard, 10 December 2007, 20:05 UTC. No auroral molecular features are present, with the exception of weak N_2^+ M(1,0) and O_2 Atm (1,1) bands at 920.0 nm and 768.0 nm, respectively; both emissions are produced by charge exchange. Auroral lines from O and O^+ are visible, indicating peak electron energy deposition at altitudes where O is abundant. The spectrum is otherwise dominated by mesospheric OH airglow bands. Strong contamination by outdoor lighting at 820.0 nm has been subtracted.

5 Data analysis and results

5.1 Optical spectra and synthetic fits

During bright auroras, high-energy (several keV) particles precipitate deep into the lower thermosphere and mesosphere, typically producing emissions from neutral and ionized N_2 and O_2. The rotational distributions from these molecular emissions indicate E-region temperatures in the lower thermosphere (a spectrum of a nighttime aurora peaking at ~110 km can be seen in Fig. 1 of Sivjee et al., 1999). In contrast, dayside and cusp auroras peak higher in the thermosphere, and are excited by $\lesssim$1 keV electrons. Optical spectra from such aurora display prominent O and O^+ emissions; electron-impacted molecular band emissions, if present, are generally very weak, precluding their use in accurately determining neutral temperatures. Fortunately, charge-exchange processes like Reaction (R1) produce thermalized rotational distributions of high-altitude ($\gtrsim$130 km) molecular species, and given sufficiently bright emissions, enable calculation of neutral temperatures (Sivjee et al., 1999).

Figure 1 shows a NIR spectrum recorded at Svalbard on 10 December 2007, which illustrates the following features typical of high-altitude aurora:

1. Mesospheric airglow OH bands dominate the spectrum. No molecular auroral emissions are discernible, with the exception of weak levels of charge-exchange produced N_2^+ M(1,0) at 910.0–930.0 nm and the R-branch

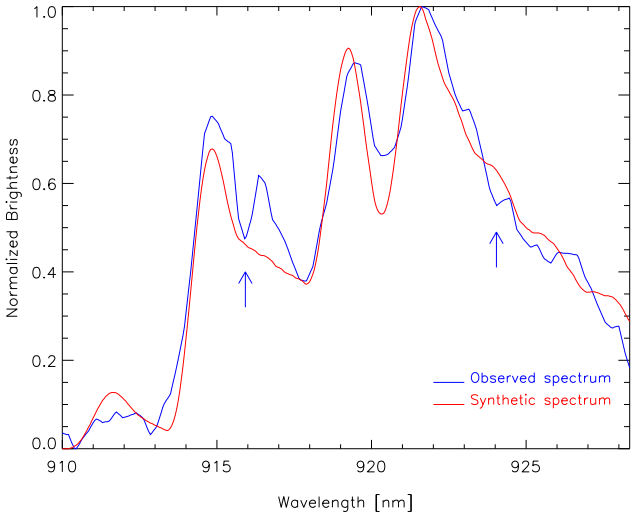

Fig. 2. A least-squares fit of the N_2^+ M(1,0) band; the rotational temperature of the synthetic spectrum is 614 K. Fitting of the observed spectrum is complicated by weak levels of the emission arising from charge exchange, contamination from overlapping non-thermalized OH emission lines, and by the presence of Fraunhofer absorption features at 916.0 nm and 922.0–925.0 nm (indicated by arrows).

peak of the O_2 Atm (1,1) at 769.0 nm. The remainder of the O_2 Atm (1,1) band is contaminated by mesospheric OH(9,4). The O_2 Atm (0,1) band (857.0–874.0 nm) is primarily an airglow feature; nevertheless, a small auroral contribution is possible.

2. The metastable O^+ 732.0–733.0 nm emission is brighter than the airglow OH(8,3) rotational lines, and there is no spectral evidence of the overlapping E-region N_2 band emissions present in the same wavelength range. The relative brightness of atomic to molecular emissions indicates precipitation of low-energy electrons.

3. Prompt oxygen auroral lines at 777.4 and 844.6 nm are visible, which, coupled with the near-absence of molecular auroral emissions, signify electron energy deposition at altitudes where O is abundant.

To determine T_n, it is first necessary to fit the rotational spectrum of the N_2^+ M(1,0) emission. This is accomplished as follows: the observed spectrum, estimates of the rotational temperature and brightness, the FWHM, and the wavelength resolution are input to a nonlinear least-squares iterative routine. Next, Hönl–London factors of the N_2^+ M(1,0) band, which determine the individual line brightness as a function of rotational temperature, are calculated using constants and expressions detailed in Kovács (1969). A synthetic spectrum is then generated by convolving the spectral lines with an instrument function defined by the FWHM, wavelength resolution, and spectral background. Finally, this procedure is iterated to minimize the least-squares difference between the observed and synthetic spectra, shown in Fig. 2.

Several difficulties arise when fitting a synthetic spectrum to the observed N_2^+ M(1,0). Chiefly, the Meinel (1,0) emission produced by charge exchange is weak and rarely exceeds 1–2 kR, unlike its lower E-region counterpart, which can exceed 45 kR (Sivjee et al., 1999). The detection of this weak emission is further compounded by the very low quantum efficiency and high noise level exhibited by silicon-based CCD chips at N_2^+ M(1,0) wavelengths.

Secondly, the (1,0) band is contaminated by the P(7)–P(11) rotational lines of the OH(7,3) band. Pendleton Jr. et al. (1993) provided evidence that these high-J number rotational levels of OH bands are non-thermalized, and do not conform to a Boltzmann rotational-vibrational distribution. When merged with another spectral feature (in our case the Meinel (1,0) emission), it is difficult to accurately determine their contribution to the brightness of the merged spectral feature. Unless the N_2^+ emission is sufficiently bright (>1 kR), the high-J number OH lines introduce uncertainties in the fitting routine.

Thirdly, spectra of Meinel (1,0) emissions originating close to the shadow height or in sunlit conditions display evidence of Swings effect, which causes a distorted spectral profile, owing to Fraunhofer absorption lines in the solar spectrum (Swings, 1941; Jones and Hunten, 1960; Deehr et al., 1980). The effect is most pronounced at 916.0 nm and in the range 922.0–925.0 nm, wavelengths corresponding to strong Fraunhofer features. Additionally, scattering of sunlight by N_2^+ ions leads to anomalous rotational and vibrational distributions (Sivjee, 1983). Both these factors hinder a more accurate least squares synthetic fit of the observed spectrum, significantly raising the uncertainty in the fitted temperature and brightness. A comprehensive error analysis taking into account resonant scattering and contamination by both Fraunhofer features and non-thermalized OH emission lines is beyond the scope of this work.

5.2 Rotational temperatures and emission altitudes

Figure 3 shows time series of N_2^+ M temperatures, and N_2^+ M and atomic oxygen brightnesses on 10 December 2007. Lagged Interplanetary Magnetic Field (IMF) components from the Advanced Composition Explorer (ACE) spacecraft and local magnetic field data from the International Monitor for Auroral Geomagnetic Effects (IMAGE) network are also plotted.

N_2^+ M temperatures and brightnesses in Fig. 3a are obtained from fitting the emission spectra, as previously discussed. Additional analysis is required to determine the brightness of the 777.4, 844.6, and 732.0 nm oxygen emissions, none of which is fully resolved from neighboring OH rotational lines. First, the rotational temperature T_{OH} of the OH(9,4), (6,2) and (8,3) bands (which overlap the 777.4, 844.6, and 732.0 nm lines, respectively) is calculated using hydroxyl lines that are fully resolved from the oxygen emissions. A knowledge of T_{OH} and the brightness of any number

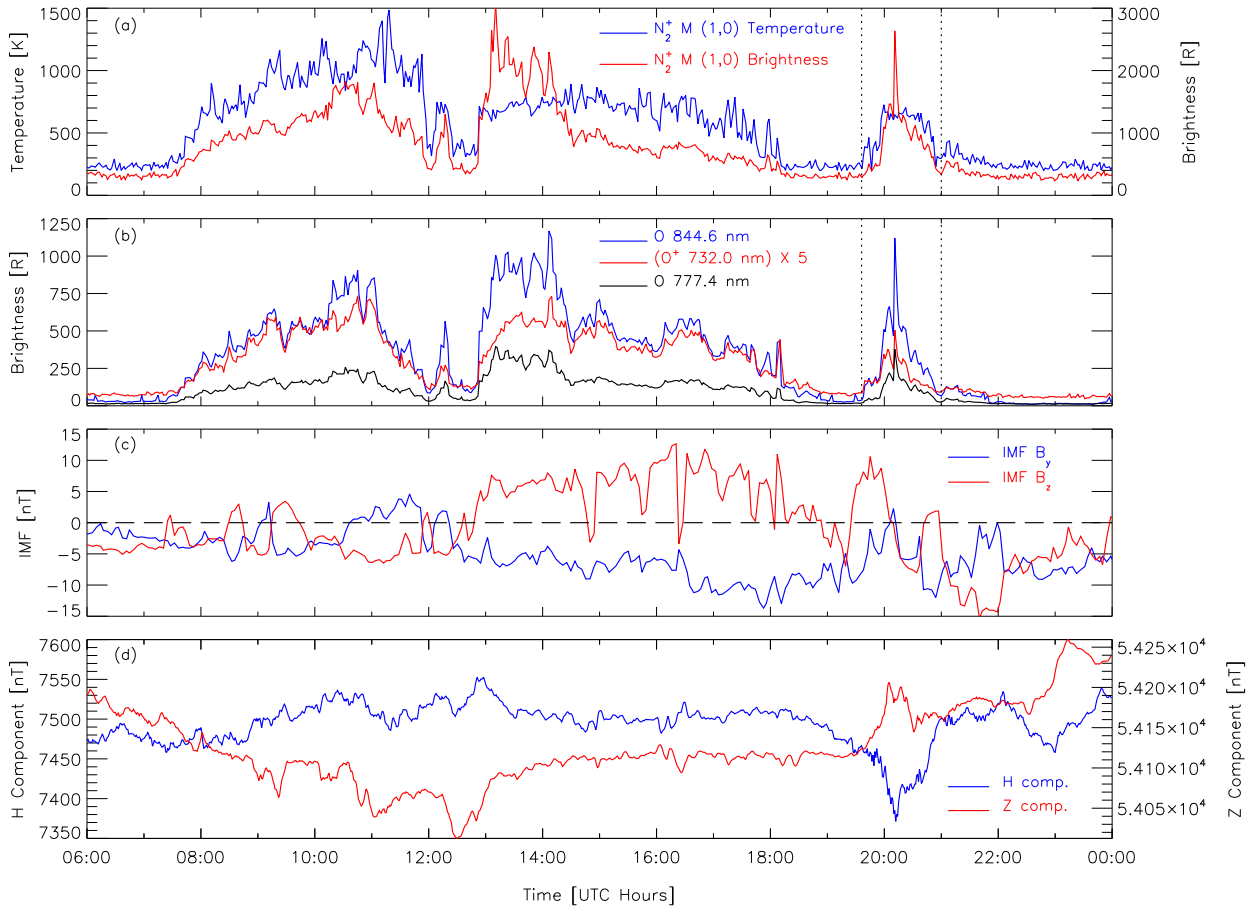

Fig. 3. Time series of optical emission data, IMF, and local magnetic field components for 10 December 2007. **(a)** N_2^+ M(1,0) rotational temperatures and brightnesses. The daytime temperatures exhibit enhancements caused by resonantly scattered sunlight. Background-subtracted brightnesses for N_2^+ M(1,0) **(a)**, and O and O^+ emissions **(b)**, all display pre- and post-local magnetic noon enhancements typically observed under the cusp (local magnetic noon occurs at 08:58 UTC). The vertical lines highlight nighttime enhancements (19:36–21:00 UTC) reproduced in Fig. 5. These enhancements are a result of increasing geomagnetic activity, as evinced by disturbed IMF and local magnetic field traces in panels **(c)** and **(d)**.

of the resolved hydroxyl lines is used to calculate the brightness of the contaminant OH rotational line, which is then subtracted from the total brightness of the merged oxygen and OH spectral feature.

The results in Fig. 3 are best discussed chronologically, focusing on two main periods, each with different N_2^+ M production methods: the cusp and dayside data from 08:00 to 18:00 UTC, and the nighttime data from 18:00 UTC onwards. Geomagnetic conditions remain relatively quiet during the former, with a_p ranging from 5 to 7. Within several hours of local magnetic noon (LMN, 08:58 UTC), Meinel rotational temperatures (Fig. 3a) rise with decreasing shadow height. Maximum values of ∼1500 K exceed atmospheric neutral temperatures, and are attained at low shadow heights of 160 km. Rotational temperatures (T_{rot}) in the range 1000–1500 K have been observed in sunlit N_2^+ 1N (Jokiaho et al., 2008), while Deehr et al. (1980) used vibrational and rotational temperatures as high as 2500 K to fit midday auroral 1N emissions. The elevated temperatures are due to resonantly-scattered photons redistributing rotational states in N_2^+ ions. Jokiaho et al. (2009) have observed that multiple scatterings can drive T_{rot} to the solar spectral temperature; clearly, under such conditions $T_{rot} \neq T_n$.

A second period of bright Meinel emissions is highlighted by vertical lines in Fig. 3a. Geomagnetic conditions were becoming increasingly disturbed: a_p, which was ≤7 for the preceding 48 h, rose to 32 at 21:00 UTC. IMF components and local magnetometer data shown in panels (c) and (d) also point to enhanced geomagnetic activity. It is possible that the nighttime enhancements in panels (a) and (b) are a sun-aligned arc, since they peak close to magnetic midnight (20:58 UTC), and appear after a sustained period of northward IMF (Ismail and Meng, 1982; Frank and Craven, 1988). N_2^+ M rotational temperatures from 20:00–20:48 UTC range between 500–700 K, with an average of 625 K. This agrees well with the 550–800 K from nighttime N_2^+ 1N emissions

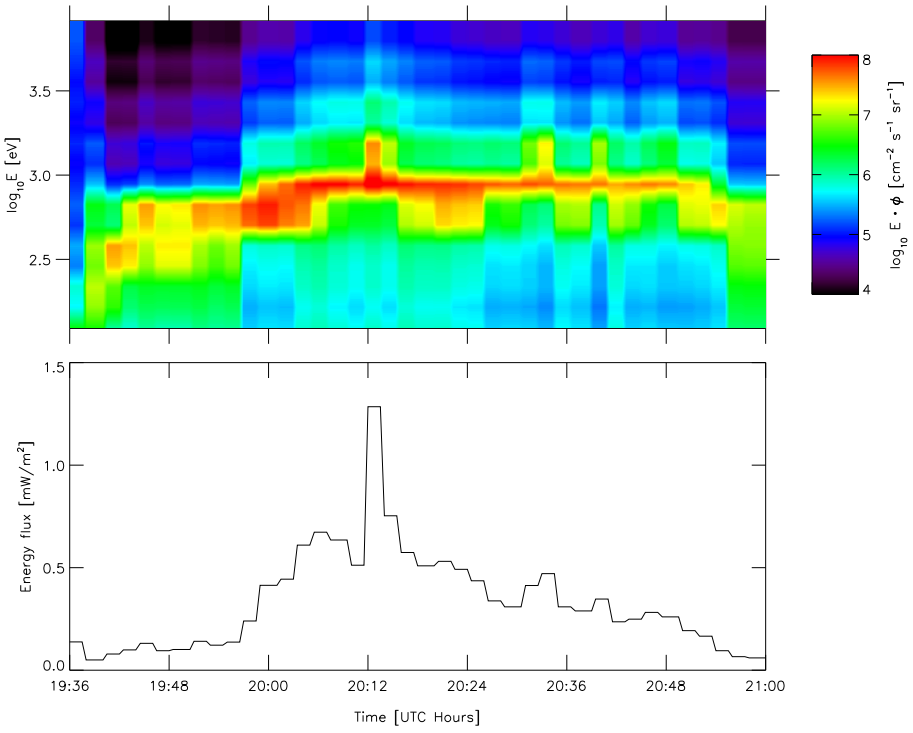

Fig. 4. (a) Energy-time spectrogram of the precipitating electron distribution, reconstructed by inverting the optical measurements in Fig. 3. Average electron energies range from 0.3–1.2 keV. The color intensities map the differential energy flux. There is a slight hardening of the electron distribution and a concurrent increase in differential energy flux starting shortly before 20:00 UTC, and gradually subsiding by 21:00 UTC. **(b)** Total hemispherical energy flux calculated from the distribution in **(a)**.

reported by Jokiaho et al. (2008). Our temperature range corresponds to an emission altitude of 135–180 km on an MSIS-90 T_n profile for similar geomagnetic conditions. Concurrent incoherent scatter radar (ISR) electron density profiles display consistent but low levels of E-region ionization peaking at 130–140 km. With the shadow height > 600 km and rising, photoionization and resonant scattering would be insignificant sources of Meinel (1,0) excitation. Thus, the nighttime emissions are excited by soft electron impact and charge exchange, and yield thermalized rotational spectra that allow the calculation of neutral temperatures. Sufficient $O^+(^2D)$, one of the reactants in Reaction (R1), is indicated by relatively high levels of the $O^+(^2P) \rightarrow O^+(^2D)$ 732.0 nm emission (Fig. 3b). The presence of this emission, which is rapidly quenched in the lower E-region, and the lack of molecular auroral emissions from direct excitation by electrons (see Fig. 1), both attest to precipitation of relatively soft electrons and emission heights of $\gtrsim$130 km.

In summary, the dayside rotational temperatures are elevated by resonantly-scattered sunlight, and are non-thermalized, yielding $T_{rot} > T_n$. This is in contrast to the thermalized nighttime emissions, produced by soft electron precipitation and charge exchange, which allow retrieval of thermospheric neutral temperatures.

5.3 Model results

To further elucidate the two nighttime N_2^+ M(1,0) production methods, TRANSCAR-derived emission brightnesses are compared to observed values. This comparison is achieved in two steps. First, as demonstrated by Zettergren et al. (2007, 2008), a time-dependent incident electron spectrum is obtained by inverting O and O^+ optical measurements at 844.6, 777.4, and 732.0 nm. N_2^+ M is not included in the inversion, since the electron-impact contribution to the emission is not initially known. Figure 4 shows the electron spectrum retrieved from the optical data. The precipitating electrons are relatively soft, with average primary energies of 0.3–1.2 keV. Starting shortly before 20:00 UTC, the number flux of the higher-energy electrons increases, with the total energy flux in Fig. 4b peaking at 20:12 UTC. It should be noted that the differential number flux (ϕ) has not been corrected for the field of view of the spectrometer. This, however, does not affect the shape of the electron spectrum, which establishes emission altitudes. The total energy flux in Fig. 4b therefore estimates the relative magnitude of the precipitating population, but should not be interpreted quantitatively.

Next, the TRANSCAR model is used to obtain emission brightnesses expected from the incident electron spectrum displayed in Fig. 4. Figure 5 shows time series of observed

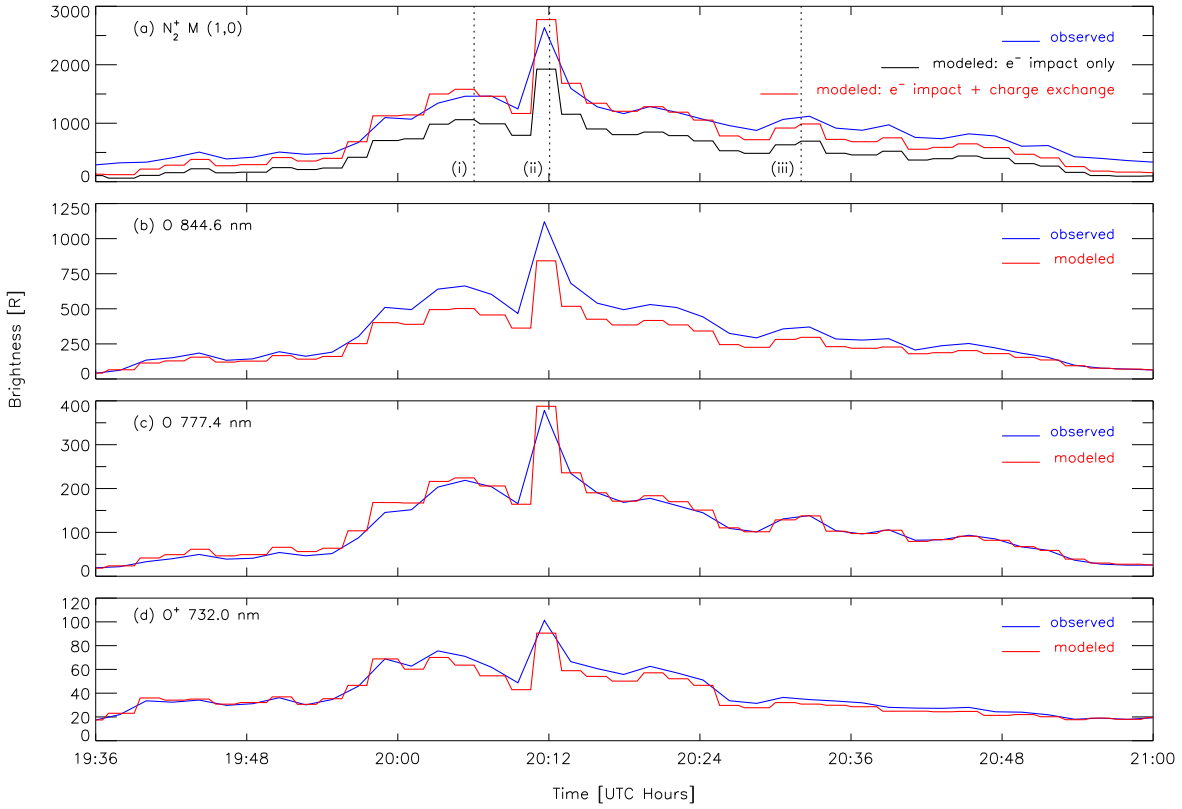

Fig. 5. Time series of observed brightnesses excerpted from Fig. 3, plotted in comparison with modeled brightnesses. Panel **(a)** shows modeled N_2^+ M emissions assuming only an electron-impact source (black line), and a combined electron-impact plus charge-exchange source (red line). The vertical lines highlight times for which volume emission rates of the two sources are plotted in Fig. 6.

and modeled brightnesses for the N_2^+ M(1,0), 844.6, 777.4, and 732.0 nm emissions, and panels (b)–(d) demonstrate good agreement between the observed and modeled data. For the N_2^+ M(1,0) emission in panel (a), however, a better agreement between the observed and modeled brightnesses is achieved upon including both electron-impact and charge-exchange mechanisms in the model. Espy et al. (1987) demonstrated that charge exchange may selectively populate the N_2^+ M(1,0) excited state during soft electron precipitation. They calculated the upper limit of the ratio p_i/p_d, where p_i = indirect production from charge exchange, p_d = direct production from electron impact, to be $1.7 \times n(O)/n(N_2)$, $n(O)$ and $n(N_2)$ being the number densities of atomic oxygen and molecular nitrogen, respectively. For the observations presented in Fig. 5, we found that $p_i/p_d = 0.8 \times n(O)/n(N_2)$ provides the best match between the observed and modeled data; applying the upper limit of Espy et al. (1987) significantly overestimates the observed brightness.

Electron impact contributes, on average, 65 % to the observed Meinel (1,0) emission. This justifies the inclusion of charge exchange as an additional production mechanism to the total auroral production rate. The volume emission rates of the two production mechanisms p_i and p_d are plotted in Fig. 6, showing their relative proportion at the three times highlighted in Fig. 5. The profiles show maximum ionization occurring in the altitude range 130–150 km, which is expected for the ∼1 keV incident electron spectrum displayed in Fig. 4 (Lummerzheim and Lilensten, 1994). Of the two mechanisms, charge exchange peaks several kilometers higher, due to the increase of $n(O)/n(N_2)$ with altitude.

6 Discussion and conclusions

In the absence of charge exchange, optical spectra obtained during soft particle precipitation display very weak molecular band emissions, if any. Nevertheless, charge-exchange reactions contribute significantly to the brightness of Meinel (1,0) and O_2 Atm (1,1) emissions, enabling the calculation of neutral temperatures from rotational spectra. There are limitations to this technique, perhaps the most significant being that the weak charge-exchange emissions exhibit low signal-to-noise ratios, thereby restricting this application to periods of enhanced brightness. Ideal conditions include a large flux of soft electrons, and for the Meinel (1,0), a dark emitting layer to prevent excitation by resonantly-scattered photons.

In this work, we have presented N_2^+ Meinel (1,0) rotational temperatures obtained during varying auroral conditions.

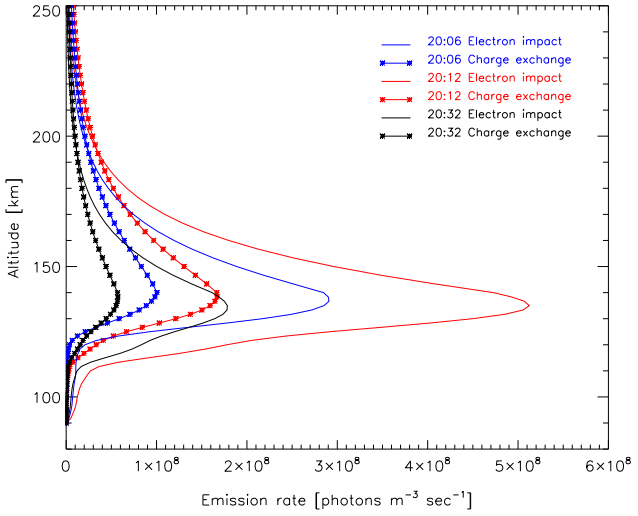

Fig. 6. Volume emission rates for two N_2^+ M(1,0) production mechanisms, charge exchange and electron impact, at 20:06, 20:12, and 20:32 UTC, respectively. The emission profiles for charge exchange peak several kilometers higher than their respective electron-impact profiles.

Time series from cusp and dayside observations, when electron impact, charge exchange, and resonant scattering all excite the emission, display rotational temperatures that exceed the asymptotic neutral temperature. The enhancements in $T_{\rm rot}$ can be attributed to resonantly-scattered photons. In contrast to the daytime observations, we infer $T_{\rm n}$ from the thermalized rotational spectra of N_2^+ M(1,0) obtained under dark skies, when both charge-exchange reactions and precipitating electrons excite the emission. The competing production mechanisms are modeled in an attempt to determine their relative contributions, and resultant emission brightnesses compare favorably with observations. Our results suggest that the charge-exchange Reaction (R1) plays a significant role in N_2^+ M(1,0) production. Furthermore, our estimated reaction rate is 50 % lower than the upper bound proposed by Espy et al. (1987). Lastly, emission heights obtained from optical data, modeling, and ISR data are consistent, and point to nighttime N_2^+ emissions emanating from ∼130 km altitude.

Several areas of investigation are possible as a continuation of this work. A detailed modeling of Reaction (R1), taking into account all production and loss channels, including ion chemistry, and important radiative and collisional losses, would better estimate the relative contributions of the different production methods. A somewhat less ambitious task would be to obtain rotational temperatures from both the O_2 Atm (1,1) at 769.0 nm, and the N_2^+ M(1,0), both of which have a charge-exchange excited component. This will yield the neutral temperature at two different heights in the thermosphere, with possible application to gravity wave studies. From an instrumentation perspective, the use of a single detector to perform multi-wavelength measurements propagates uncertainties in the fitting of rotational spectra, in the calculation of the precipitating electron distribution, and ultimately in the modeled brightnesses. Since retrieving the electron spectrum requires inverting optical brightnesses obtained at several wavelengths, a possible improvement would be a multi-instrument approach, with each optimized for a particular emission.

In conclusion, in both lower E-region auroras and in higher-altitude auroras, $T_{\rm n}$ in the latter typically cannot be obtained from auroral molecular spectra normally employed for temperature determination in the former. We have demonstrated an exception to this, and shown how charge exchange produces thermalized rotational populations at altitudes of ∼130 km, from which it is possible to obtain $T_{\rm n}$. This technique represents an additional means of remotely sensing the neutral atmosphere.

Acknowledgements. This work was supported by grants NSF ATM-0854704 and NSF ATM-0449864. M. D. Zettergren acknowledges the support of NSF grant AGS-1000302. IMAGE Magnetometer data was obtained from Tromsø Geophysical Observatory, University of Tromsø. We thank the staff at the Kjell Henriksen Observatory for their support, and acknowledge the ACE SWEPAM instrument team and the ACE Science Center for availing the ACE IMF data.

Topical Editor L. Blomberg thanks D. Lummerzheim and one anonymous referee for their help in evaluating this paper.

References

Angell, J. K. and Korshover, J.: Global temperature variations in the troposphere and stratosphere, 1958–1982, Mon. Weather Rev., 111, 901–921, 1983.

Blelly, P.-L., Lilensten, J., Robineau, A., Fontanari, J., and Alcaydé, D.: Calibration of a numerical ionospheric model with EISCAT observations, Ann. Geophys., 14, 1375–1390, doi:10.1007/s00585-996-1375-x, 1996.

Broadfoot, A.: Resonance scattering by N_2^+, Planet. Space Sci., 15, 1801–1815, 1967.

Broadfoot, A. L. and Stone, T.: The N_2 + O^+ charge-exchange reaction and the dayglow N_2^+ emission, J. Geophys. Res., 104, 17145–17155, 1999.

Chamberlain, J. W.: Physics of the aurora and airglow, Academic Press Inc., New York, United States, 1961.

Chanin, M. L. and Hauchecorne, A.: Lidar observation of gravity and tidal waves in the stratosphere and mesosphere, J. Geophys. Res., 86, 9715–9721, 1981.

Deehr, C. S., Sivjee, G. G., Egeland, A., Henriksen, K., Sandholt, P. E., Smith, R., Sweeney, P., Duncan, C., and Gilmer, J.: Ground-based observations of *F* region aurora associated with the magnetospheric cusp, J. Geophys. Res., 85, 2185–2192, 1980.

Diloy, P.-Y., Robineau, A., Lilensten, J., Blelly, P.-L., and Fontanari, J.: A numerical model of the ionosphere, including the E-region above EISCAT, Ann. Geophys., 14, 191–200, doi:10.1007/s00585-996-0191-7, 1996.

Espy, P. J., Pendleton, Jr, W. R., Sivjee, G. G., and Fetrow, M. P.: Vibrational development of the N_2^+ Meinel band system in the aurora, J. Geophys. Res., 92, 11257–11261, 1987.

Frank, L. A. and Craven, J. D.: Imaging results from Dynamics Explorer 1, Rev. Geophys., 26, 249–283, 1988.

Hedin, A.: Extension of the MSIS thermosphere model into the middle and lower atmosphere, J. Geophys. Res., 96, 1159–1172, 1991.

Henriksen, K.: N_2^+ emissions in sunlit cusp and night-side aurora, Ann. Geophys., 2, 457–462, 1984.

Henriksen, K., Veseth, L., Deehr, C. S., and Smith, R. W.: Neutral temperatures and emission height changes in an *E*-region aurora, Planet. Space Sci., 35, 1317–1321, 1987.

Hernandez, G.: Lower-Thermosphere temperatures determined from the line profiles of the OI 17,924-K (5577 Å) emission in the night sky, 1. Long-term behavior, J. Geophys. Res., 81, 5165–5172, 1976.

Hocking, W. K. and Hocking, A.: Temperature tides determined with meteor radar, Ann. Geophys., 20, 1447–1467, doi:10.5194/angeo-20-1447-2002, 2002.

Ismail, S. and Meng, C. I.: A classification of polar cap auroral arcs, Planet. Space Sci., 30, 319–330, 1982.

Jokiaho, O., Lanchester, B. S., Ivchenko, N., Daniell, G. J., Miller, L. C. H., and Lummerzheim, D.: Rotational temperature of N_2^+ (0,2) ions from spectrographic measurements used to infer the energy of precipitation in different auroral forms and compared with radar measurements, Ann. Geophys., 26, 853–866, doi:10.5194/angeo-26-853-2008, 2008.

Jokiaho, O., Lanchester, B. S., and Ivchenko, N.: Resonance scattering by auroral N_2^+: steady state theory and observations from Svalbard, Ann. Geophys., 27, 3465–3478, doi:10.5194/angeo-27-3465-2009, 2009.

Jones, A. V. and Hunten, D. M.: Rotational and vibrational intensity distribution of the first negative bands in sunlit auroral rays, Can. J. Phys., 38, 458–476, 1960.

Keckhut, P., Wild, J. D., Gelman, M., Miller, A. J., and Hauchecorne, A.: Investigations on long-term temperature changes in the upper stratosphere using lidar data and NCEP analyses, J. Geophys. Res., 106, 7937–7944, 2001.

Kelly, J.: Sondrestrom radar – Initial results, Geophys. Res. Lett., 10, 1112–1115, 1983.

Killeen, T. L., Won, Y. I., Niciejewski, R. J., and Burns, A. G.: Upper thermosphere winds and temperatures in the geomagnetic polar cap: Solar cycle, geomagnetic activity, and interplanetary magnetic field dependencies, J. Geophys. Res., 100, 21327–21342, 1995.

Koehler, R. A., Shepherd, M. M., Shepherd, G. G., and Paulson, K. V.: Rotational temperature variations in pulsating auroras, Can. J. Phys., 59, 1143–1149, 1981.

Kovács, I.: Rotational structure in the spectra of diatomic molecules, Vol 1, Adam Hilger, London, UK, 1969.

Kvifte, G.: Temperature measurements from OH bands, Planet. Space Sci., 5, 153–157, 1961.

Lilensten, J. and Blelly, P.-L.: The TEC and F2 parameters as tracers of the ionosphere and thermosphere, J. Atmos. Solar-Terr. Phys., 64, 775–793, doi:10.1016/S1364-6826(02)00079-2, 2002.

Lummerzheim, D. and Lilensten, J.: Electron transport and energy degradation in the ionosphere: evaluation of the numerical solution, comparison with laboratory experiments and auroral observations, Ann. Geophys., 12, 1039–1051, doi:10.1007/s00585-994-1039-7, 1994.

Matuura, N., Masuda, Y., Inuki, H., Kato, S., Fukao, S., Sato, T., and Tsuda, T.: Radio acoustic measurement of temperature profile in the troposphere and stratosphere, Nature, 323, 426–428, 1986.

Meinel, A. B.: A new band system of N_2^+ in the infrared auroral spectrum, Astrophys. J., 112, 562–563, 1950.

Omholt, A.: The red and near-infra-red auroral spectrum, J. Atmos. Terr. Phys., 10, 320–331, 1957.

Pendleton Jr., W. R., Espy, P. J., and Hammond, M. R.: Evidence for non-local-thermodynamic-equilibrium rotation in the OH nightglow, J. Geophys. Res., 98, 11567–11579, 1993.

Petrie, W.: Rotational temperatures of auroral nitrogen bands, J. Atmos. Terr. Phys., 4, 5–6, 1953.

Revathy, K., Nair, S. R. P., and Murthy, B. V. K.: Deduction of temperature profile from MST radar observations of vertical wind, Geophys. Res. Lett., 23, 285–288, 1996.

Romick, G. J., Degen, V., Stringer, W. J., and Henriksen, K.: The altitude profile of the N_2^+ First Negative rotational temperature in an auroral arc, J. Geophys. Res., 83, 91–96, 1978.

She, C. Y., Yu, J. R., and Chen, H.: Observed thermal structure of a midlatitude mesopause, Geophys. Res. Lett., 20, 567–570, doi:10.1029/93GL00808, 1993.

Sigernes, F., Holmes, J. M., Chernouss, S., Svenøe, T., Dyrland, M., Lorentzen, D. A., Moen, J., and Deehr, C. S.: Sensitivity calibration of narrow field of view optical instruments, http://kho.unis.no/doc/Sigernes_Calibrate.pdf, 2007.

Sivjee, G. G.: Differences in near UV (∼3400−4300 Å) Optical emissions from midday cusp and nighttime auroras, J. Geophys. Res., 88, 435–441, 1983.

Sivjee, G. G. and Hamwey, R. M.: Temperature and chemistry of the polar mesopause OH, J. Geophys. Res., 92, 4663–4672, 1987.

Sivjee, G. G., Shen, D., Yee, J.-H., and Romick, G. J.: Variations, with peak emission altitude, in auroral O_2 atmospheric (1,1)/(0,1) ratio and its relation to other auroral emissions, J. Geophys. Res., 104, 28003–28018, 1999.

Swings, P.: Complex structure of cometary bands tentatively ascribed to the contour of the solar spectrum, Lick Observatory Bulletin, 19, 131–136, 1941.

Vallance Jones, A.: Aurora, D. Reidel, Dordrecht, Netherlands, 1974.

Vallance Jones, A., Gattinger, R. L., Shih, P., Meriwether, J. W., Wickwar, V. B., and Kelly, J.: Optical and radar characterization of a short-lived auroral event at high latitude, J. Geophys. Res., 92, 4575–4589, 1987.

Vegard, L.: The temperature of the auroral region determined by the rotational series of the negative nitrogen-bands, Terrestrial Magnetism and Atmospheric Electricity, 37, 389–398, doi:10.1029/TE037i003p00389, 1932.

Zettergren, M.: Model-based optical and radar remote sensing of transport and composition in the auroral ionosphere, Ph.D. thesis, Boston University, 2009.

Zettergren, M., Semeter, J., Blelly, P.-L., and Diaz, M.: Optical estimation of auroral ion upflow: Theory, J. Geophys. Res., 112, A12310, doi:10.1029/2007JA012691, 2007.

Zettergren, M., Semeter, J., Blelly, P.-L., Sivjee, G., Azeem, I., Mende, S., Gleisner, H., Diaz, M., and Witasse, O.: Optical estimation of auroral ion upflow: 2. A case study, J. Geophys. Res., 113, A07308, doi:10.1029/2008JA013135, 2008.